



HAL
open science

Cold Sintering Process characterization by in operando electrochemical impedance spectroscopy

Thomas Hérisson de Beauvoir, Pierre-Louis Taberna, Patrice Simon, Claude Estournès

► **To cite this version:**

Thomas Hérisson de Beauvoir, Pierre-Louis Taberna, Patrice Simon, Claude Estournès. Cold Sintering Process characterization by in operando electrochemical impedance spectroscopy. *Journal of the European Ceramic Society*, 2022, 42 (13), pp.5747-5755. 10.1016/j.jeurceramsoc.2022.05.077 . hal-03799854

HAL Id: hal-03799854

<https://hal.science/hal-03799854>

Submitted on 26 Mar 2024

HAL is a multi-disciplinary open access archive for the deposit and dissemination of scientific research documents, whether they are published or not. The documents may come from teaching and research institutions in France or abroad, or from public or private research centers.

L'archive ouverte pluridisciplinaire **HAL**, est destinée au dépôt et à la diffusion de documents scientifiques de niveau recherche, publiés ou non, émanant des établissements d'enseignement et de recherche français ou étrangers, des laboratoires publics ou privés.

Cold Sintering Process characterization by *in operando* Electrochemical Impedance Spectroscopy

Thomas Hérisson de Beauvoir, Pierre-Louis Taberna, Patrice Simon, Claude Estournès

CIRIMAT, CNRS-INP-UPS, Université Toulouse 3 – Paul Sabatier, 118 route de Narbonne, 31062 Toulouse, France

Abstract:

The development of *in situ* characterization techniques is mandatory for the development of the Cold Sintering Process (CSP). Here we show the first development of *in situ* impedance analyzes to follow materials evolution during sintering. This characterization brings key information about grain boundary formation at the solid/liquid interface, both in terms of thermodynamic and kinetics. Through the example of ZnO sintering in the presence of acetic acid aqueous solution, known for being easily Cold Sintered, we demonstrate the role of the liquid phase, notably the acetic acid role, regarding chemical composition, structure and microstructure of the obtained densified ceramics. It turns out this is a promising in-situ characterization technique that should be applied to a wide range of materials.

1. Introduction

The recent development of the low temperature sintering techniques, well represented by the Cold Sintering Process (CSP) [1], has been found to be an efficient way to achieve high density ceramics [2], within short sintering times (few minutes to few hours). In most cases, the process relies on a mix of a powder and a liquid phase (most often aqueous), set in a die and heated under uniaxial pressure. While CSP was successfully applied to a wide range of materials [1], leading to dense samples using a single step sintering process, it remains challenging and sometimes leads to incomplete densification [3]. In many cases, CSP is used as a pre-sintering step, leading to better grain to grain contacts, followed by a high temperature treatment to complete material's sintering [4–6]. This is thus a two-step sintering process. In that case, the CSP pre-treatment allows an important sintering temperature reduction compared to non CSP-treated samples. Although it allows a reduction of the sintering temperature (few hundred degrees) and is therefore interesting in some cases, using such high temperature post annealing limits the intrinsic interests of CSP, since it may decompose organic-polymer phases or induce crystalline phase transition of ceramics.

To overcome this issue, it is necessary to develop fundamental understanding of sintering mechanisms involved to achieve better densification in CSP and avoid further heat treatment.

Some authors investigated the application of existing liquid phase sintering mechanisms models on the CSP of some materials such as SiO₂ and ZnO [7]. Their work has demonstrated that the involved mechanisms are more complex than those of conventional liquid phase sintering. They have shown that along solid/liquid interfaces, multiple mechanisms may occur: secondary phase formation, surface defects formation and/or recrystallization. Therefore, to refine sintering models, suitable characterization techniques are needed, especially to bring new insights regarding the solid/liquid interface reactivity. Indeed, among the obvious energy consumption reduction arising from temperature and time reduction, lowering the sintering temperatures opens new opportunities in terms of materials nature that can be sintered, including composites. This way, various ceramic/polymer and ceramic/metal composite systems have been sintered, exhibiting different interfaces, inducing modified reactivity [8]. More recently, grain boundary engineering has been used in CSP by adding polymer or chelating agents to control grain growth/morphology [9–11]. These may promote grain growth inhibition and, in other cases, grain nucleation. Using organic compounds at the interfaces of sintering ceramic powders remains challenging to characterize since a very limited amount may be needed, and no technique allows their direct characterization. It is thus necessary to design *in situ* characterizations for the development of sintering theoretical models to better understand and control the Cold Sintering Process. Recently, Allen *et al.* [12] have developed a setup to perform *in situ* XRD characterization (USAXS, SAXS and WAXS) to follow porosity and crystallization at solid/liquid interfaces. This setup reports for the first time a real-time, non-destructive characterization of Cold Sintering Process.

Another possibility to characterize the sintering mechanisms involved in CSP experiment consists in measuring the electrical properties of samples while they are sintering. Electrochemical Impedance Spectroscopy (EIS) is widely used for the characterization of electroceramics [13]. It allows the separation of the various material's contributions to electrical properties depending of the measuring frequency. This way, one can discriminate the contribution of grains and grain boundary interfaces [13–15] in a ceramic. The interests of using such characterization techniques during CSP experiments consist in: i) the non-destructive nature of electrical characterization, ii) the short measurement time required and iii) the use of electrically conductive sintering setup allows good current collection (WC, stainless steel or graphite dies are mostly used for CSP), further aided by the application of uniaxial pressure, favoring a good electrical contact between the sample and the electrodes. However, the main limit to the use of such techniques deals with the impedance range which

is experimentally measurable, and is not applicable to purely resistive nor conductive samples. In the present work, we focused on the sintering of ZnO ceramics by CSP in the presence of acetic acid aqueous solution. It has multiple assets that make it a good candidate for the development of *in situ* electrochemical impedance spectroscopy characterization. First, it has proved great sintering efficiency at low temperatures (below 300 °C), reaching > 99% density in CSP [2,16]. Additionally, ZnO is an intrinsic electronic n-type semi-conductor, which can be characterized by EIS measurements [14,17–19]. Eventually, its high ability to densify at low temperatures makes it an interesting material for developing and testing sintering models [7,20]. Therefore, it is among the most present cold sintered material in literature, and EIS data bring key insight in developing sintering models. Moreover, Jing *et al.* have shown a strong influence of cold sintering conditions on the electrical properties of ZnO in acetic acid. They have demonstrated 5 orders of magnitude electrical conductivity increase of cold sintered ZnO samples after 500 °C annealing in Ar compared to as cold sintered samples [21]. *In situ* electrical measurements offer the opportunity to determine whether the conditions favor some specific reactivity, eventually allowing to control material's properties.

2. Experimental

The ZnO was obtained from Alfa Aesar (99%) with particle size of 40-100 nm and acetic acid from Sigma Aldrich (>99%). Acetic acid was mixed with pure water to prepare 1 M solution. For the sintering experiments, 3 g of powder were mixed with 0.28 mL of 1 M acetic acid solution and manually mixed in a mortar. After 5 min of mixing, the powder was added to a 20 mm diameter WC die. To prevent direct contact between the die and the powder, a graphite foil was placed between the powder and each punch, and the inner part of the die was covered with Kapton foil to prevent direct electrical contact between the die and the sample. An uniaxial pressure was applied and maintained constant throughout sintering process with an Atlas T25 automated hydraulic press to 100 MPa for all experiments. Temperature and sintering time for the various samples prepared are described in the results section. After sintering, graphite foils were removed manually with a razor and sample surfaces were polished to remove graphite residues on surfaces before further characterizations could be performed. *In situ* electrochemical impedance spectroscopy (EIS) measurements were achieved using a M² 7260 impedance analyzer in the frequency range 10 Hz - 1 MHz under an AC voltage of 100 mV. Each measuring cycle took 40 sec, and a 20 sec break was applied before the next measurement. This way, one measurement per minute could be recorded. The electrodes consisted in stainless-steel plates put into contact with the extern part of both

punches. Electrical data were fitted with the Zview software (from Scribner Associates) using series R-CPE equivalent circuit. Density measurements were first done geometrically and further measured by Archimedes' method (using water). The first measurement was used to check whether open porosity was present and the former was used for data plots in the following. SEM observations were done with a TESCAN Vega 3 microscope using 10 kV acceleration voltage on fractured samples. XRD analyzes were achieved using a Bruker D4 Endeavor diffractometer with Cu-K α radiation on 30-65° (2 θ range), on both polished surfaces and powders obtained from crushed sintered pellets. Raman spectroscopy was done using a Labram HR 800 Yvon Jobin confocal Raman spectrometer equipped with a 532 nm laser. For each sample, a minimum of 3 different zones were randomly chosen and measured. The data provided in the following correspond to an average value of these measurements, and the error bars correspond to their standard deviation. Calibration was done before any measurement session using a Si single crystal. Thermo Gravimetric Analyzes were performed with a Setaram TAG16 equipment with a 10 °C/min thermal ramp from room temperature to 600 °C under air atmosphere.

3. Results

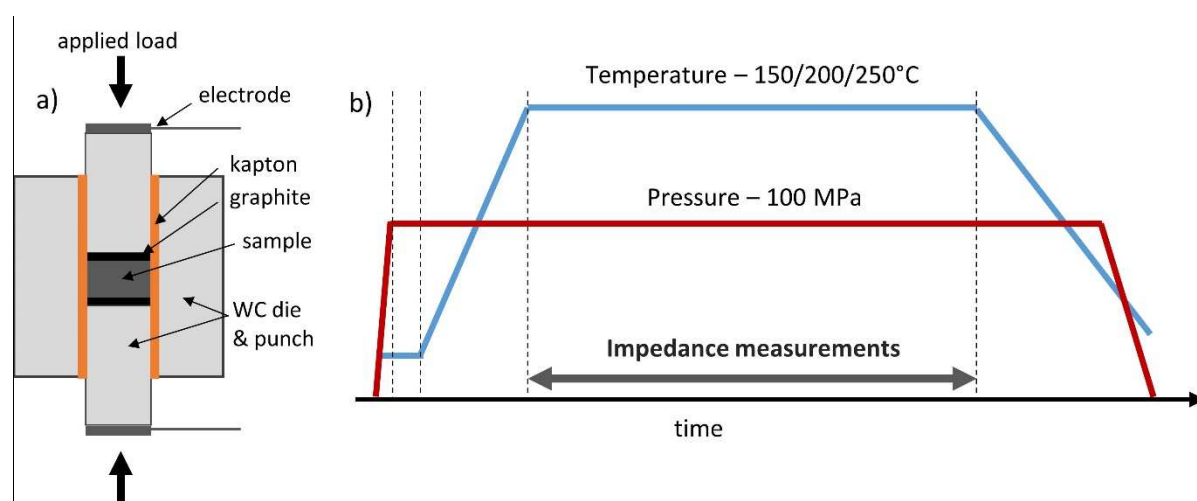


Figure 1: a) Schematic representation of the experimental die setup and b) temperature and pressure profile.

Electrical measurements are performed during the sintering dwell time.

To achieve electrical measurements during sintering, the experimental setup was adapted as presented in Figure 1a. Electrodes were placed on the external surface of both punches (top and bottom), and a Kapton sheet is placed around the sample, on the inner die surface to electrically insulate the sample (being measured) from the die. The pressure and temperature profiles are described on Figure 1b. Pressure was first applied to 100 MPa within 5 s at room temperature. After 1 min, temperature was increased to the sintering temperature (150 °C,

200 °C and 250 °C) with a thermal ramp ranging from 40 to 20 °C/min (see Figure S1). Temperature was finally decreased to room temperature under constant pressure, which was released after 15 min of cooling. EIS measurements were registered every minute during that whole sintering time at constant temperature.

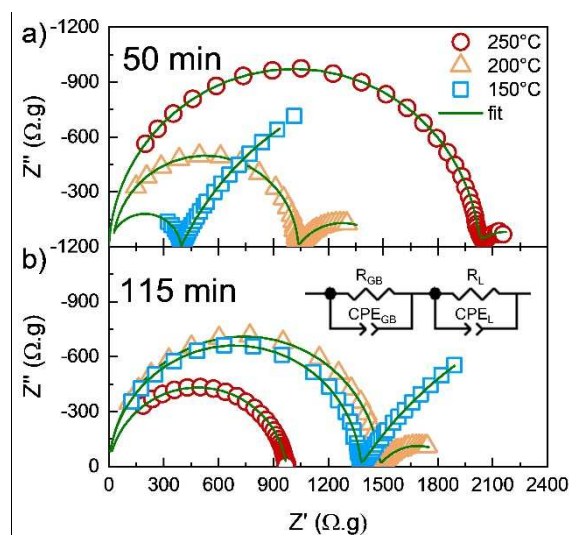


Figure 2: Nyquist plots of in situ electrochemical impedance measurements data for three ZnO samples cold sintered at various temperatures (150, 200 and 250 °C) with 1M acetic acid aqueous solution after a) 50 min and b) 115 min sintering time. Inset represents the equivalent circuit used for data fitting, considering GB as grain boundaries and L as the liquid phase.

Typically obtained data are displayed on Figure 2 for two different sintering times (at 50 min on a) and 115 min on b). The experimental setup used does not allow the measurement of axial displacement (i.e. densification kinetics). Thus, we do not have access to the real-time density/sample geometry. To compare various samples' impedance data, they were multiplied by the sample's mass, which is the same for all samples throughout this manuscript (3g of solid ZnO for all samples). After 50 min (Figure 2a), two incomplete semi-circles can be observed on the Nyquist plots for the three samples, as the frequency range was not broad enough to get them complete. After 115 min, while the two lower temperature samples (150 and 200 °C) still exhibit two semi-circles, a single one is observed at 250 °C, showing that the ceramic turns conductive at low frequency (conductive pathway through the sample). Based on the brick-layer model, usual applied for electroceramics, [22] (used in the case of ZnO-based varistor ceramics [14]) data were fitted using an R-CPE for each semi-circle, both connected in series. Data fitting was done for the three samples at the various sintering times. Three main semi-circles are expected to be observed, arising from the contributions of grains, grain boundaries and/or liquid phase (aqueous solution of acetate and dissolved zinc ions).

The room temperature impedance diagrams, measured after sintering for all three samples, are displayed on Figure S2. All samples exhibit two relaxations (Z'' peaks on Figure S2b). A relaxation is observed for all samples around 10 to 50 kHz, which can be attributed to ZnO grain boundaries. For the 250°C sample, a second semi-circle is visible at higher frequency (>1 MHz) (see Figure S2 a and b) which can be expected for the bulk part of ZnO. The impedance magnitude for the 150 and 200°C samples is 3 orders of magnitude higher than for 250°C sample, thus the bulk contribution cannot be observed. However, another contribution is visible < 100 Hz which is attributed to the liquid phase. When temperature increases, relaxation frequencies of each contribution increases, and the bulk contribution is out of the measurement range. Thus, the observed semi-circles on Figure 2 are attributed to the grain boundaries (GB) and the liquid phase (L). The fitted resistances for all samples and plotted on Figure 3 both for the GB and L semi-circles.

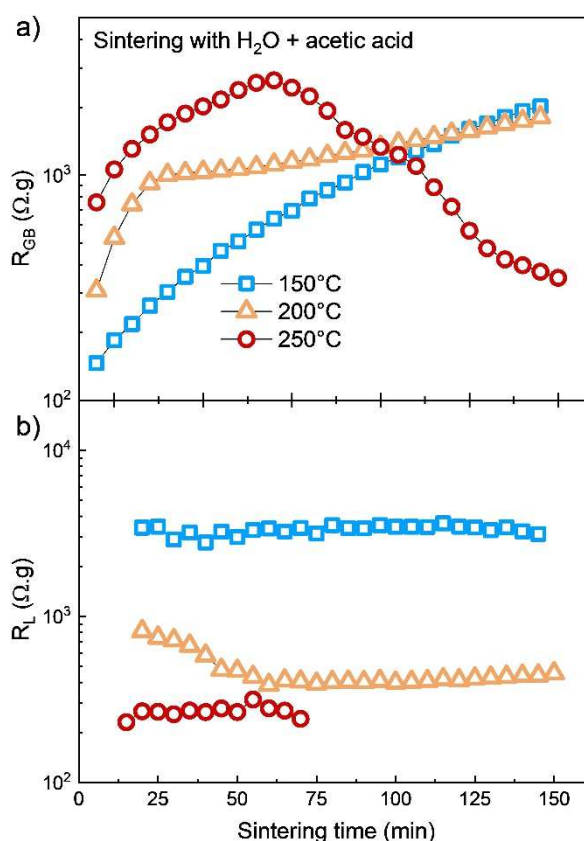


Figure 3: Fitted resistances for both a) grain boundary (GB) and b) liquid phase (L) semi-circles.

According to Figure 3a, R_{GB} initially increases with time for the three samples. While it increases during the whole sintering time for the samples sintered at 150 and 200 °C, it suddenly decreases for the 250 °C sample from 70 to 150 min. At the end of the sintering time (150 min) the 150 and 200 °C samples have similar R_{GB} (2.2 and 1.8 kΩ.g, respectively),

while the 250 °C sample has a much lower R_{GB} of 0.3 k Ω .g. According to Figure 3b, R_L remains stable for the 150 °C sample around 3 to 3.2 k Ω .g over the whole sintering dwell time. At 200 °C, it initially decreases from 0.8 to 0.4 k Ω .g during the first 70 min, then remains stable. In the case of sintering at 250 °C, R_L is first stable during 70 min at 0.25 k Ω .g, then totally vanishes, as visible on Figure 2b (115 min) where only R_{GB} semi-circle is observed. The sample becomes conductive at low frequency, probably related to liquid elimination. The same measurements were made on dry ZnO powder (named dry), as well as on ZnO mixed with distilled water, without acetic acid (named H₂O) during sintered at 250 °C. The resulting data are presented on Figure 4.

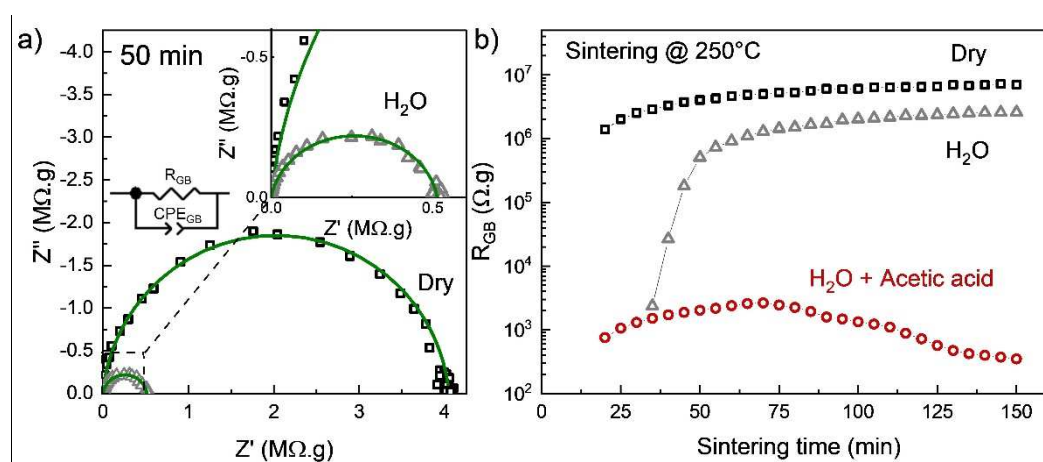


Figure 4: a) Nyquist plots obtained from in situ electrochemical impedance measurement at 250°C on dry ZnO powder and ZnO with H₂O (a magnified view is presented in inset). Green lines represent their data fitting using a single R-CPE model. b) Fitted resistances for pure ZnO powder (dry), ZnO with H₂O and compared with R_{GB} of ZnO with H₂O and acetic acid taken from figure 3a. Relative densities of samples after the sintering process are 59.9% (dry), 83.4% (H₂O) and 99.1% (H₂O + Acetic acid).

The Nyquist plots of both dry ZnO powder (dry) and ZnO mixed with H₂O are presented on Figure 4a. Both exhibit a single semi-circle, which can be well fitted using an R-CPE equivalent circuit, as the one used previously. The fitted resistance data are plotted on Figure 4b and compared with R_{GB} data of the sample sintered with acetic acid at 250 °C presented earlier. The absence of a second semi-circle at lower frequency confirms that it arises from acetate species. Thus, only the grain boundary contribution to impedance is visible. The evolution of both samples (dry and H₂O) without acetic acid shows a R_{GB} increase followed by a plateau at 2.3 M Ω .g for H₂O sample and 6.5 M Ω .g for the dry sample. These values are few orders of magnitude higher than those measured on the sample containing acetic acid (< 3 k Ω .g) and follow a constant R_{GB} evolution during sintering (oppositely to the R_{GB} evolution of the sample containing acetic acid sintered at the same temperature). The role of

acetic acid on the densification of ZnO during cold sintering has been studied [23]. Initially, it creates a hydroxide layer on the ZnO solid surfaces, and promotes Zn^{2+} dissolution. By creating chelated complex of Zn^{2+} with acetates in the liquid phase, it is then possible to diffuse Zn^{2+} from the grain boundary region to the nearby porosities. Then, Zn^{2+} can bind to bridging hydroxydes on the surfaces of ZnO in porosities with lowered activation energy. These mechanisms, creating vacancy-rich (V_{Zn}) and hydroxylated surfaces allows fast surface diffusion, further leading to efficient densification. The acetate species both participate to the dissolution, but also lower the activation energy of surface diffusion. For these reasons, densification is strongly increased in the presence of acetate species in contrast to pure water [16].

To investigate the effect of increasing sintering time on the evolution of R_{GB} , a sample was sintered at 200 °C during 360 min and compared to the sample sintered at the same temperature for 150 min. The results are displayed on Figure S3, and confirm a constant logarithmic evolution of R_{GB} with sintering time. This observation tends to confirm that the R_{GB} decrease, observed for the sample sintered at 250 °C, cannot be reproduced simply with longer sintering time, and that some mechanism must be activated between 200 and 250 °C in the presence of acetic acid, explaining the electrical properties evolution.

To check whether the R_{GB} evolution at 250 °C may originate from structural or microstructural modification, the obtained pellets were first characterized by density measurements.

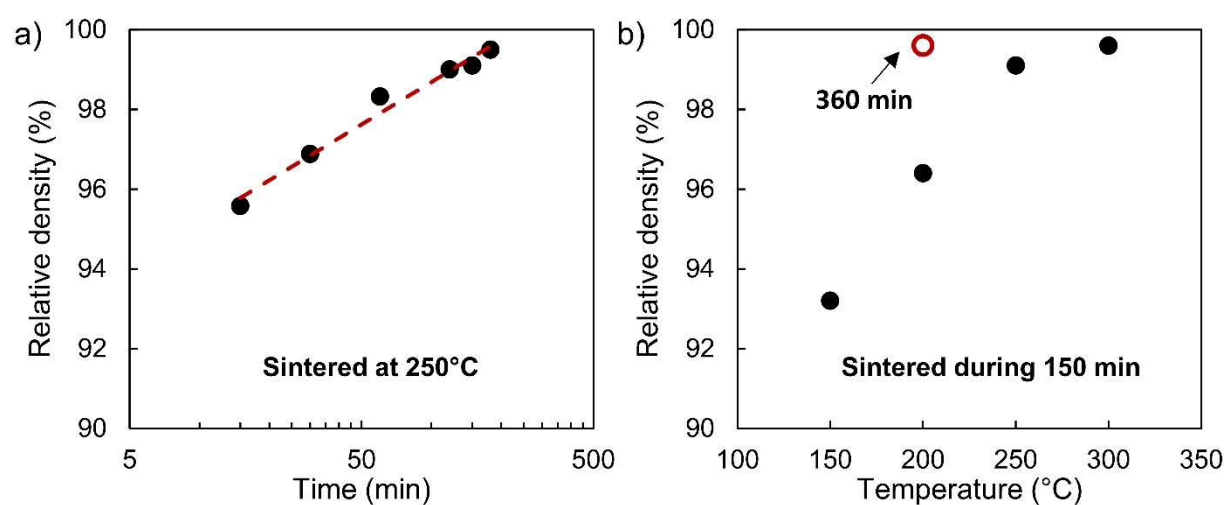


Figure 5: Relative densities measured on sintered samples a) at fixed temperature and varying time, and b) fixed time and varying temperatures. Orange empty circle corresponds to a sample sintered at 200 °C during 360 min.

On Figure 5 are presented samples relative densities for different sintering times at 250 °C (Figure 5a), and samples sintered during 150 min at various temperatures (Figure 5b). As expected, relative density increases both with higher sintering temperature and dwell time. However, it can be noticed that sample sintered at 250 °C for 15 min already exhibits a relative density higher than 95%. The evolution of the relative density with sintering temperature (and constant dwell time of 150 min) shows that complete densification is not reached for the three samples sintered at 150, 200 and 250 °C, while a density > 99% can be obtained at 300 °C. The EIS measurements of the sample sintered at 300 °C are not presented since the conductivity was too high for proper analysis. However, the sample sintered at 200 °C for 360 min (represented as an orange empty dot in Figure 5b) has a relative density of 99.6%, higher than 250 °C – 150 min (99.1%). This suggests that electrical properties evolution at 250 °C – 70 min does not arise only from densification level.

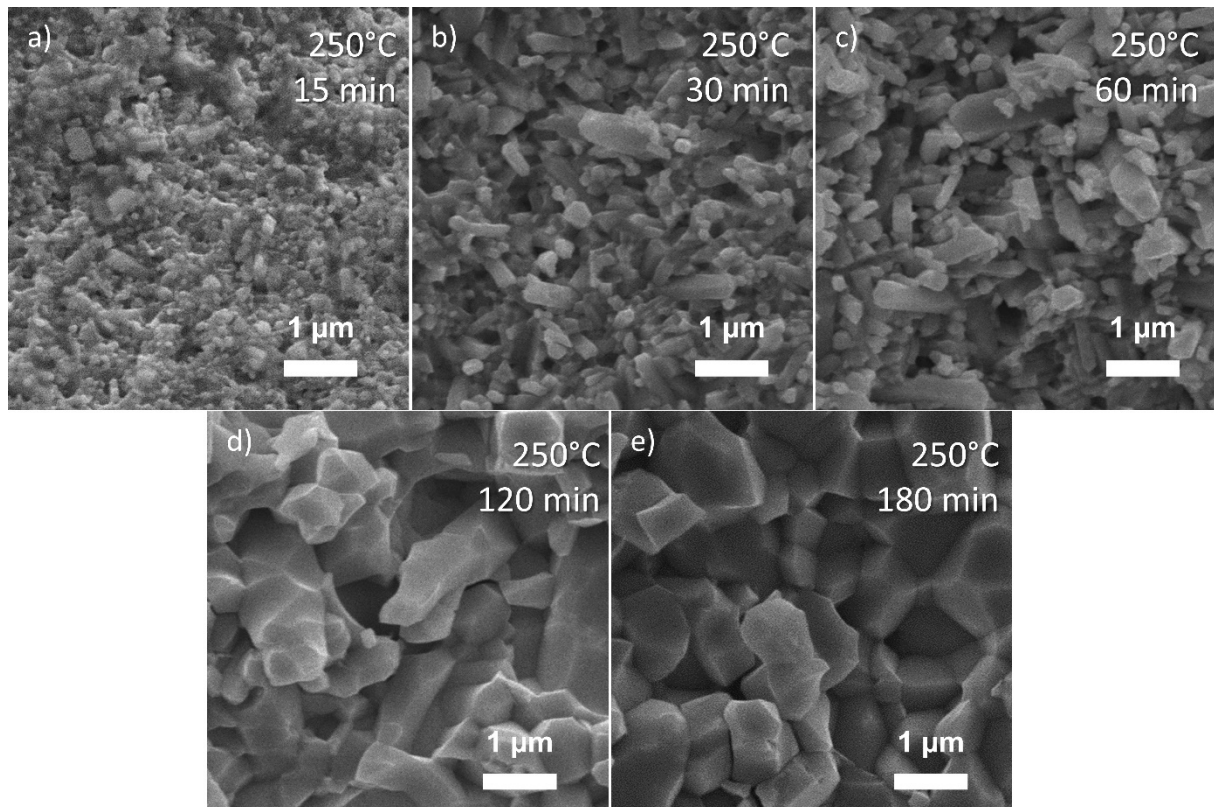


Figure 6: SEM observations on fractured samples sintered at 250 °C a-e) 15 to 180 min

To explore the possible microstructural origin of electrical properties evolution at 250 °C, SEM observations of samples prepared at various sintering times were performed (see Figure 6). These microstructures show very low porosity, confirming the measured samples density, and show increasing grain sizes when sintering time increases, as expected. Moreover, they exhibit mainly elongated shapes for the lower sintering times (≤ 60 min), and more isotropic

shapes when time increases (120 and 180 min). It is well known that zinc acetate plays a role in the formation of ZnO needles, growing along the c axis of wurtzite structure, especially in warm and humid conditions [24]. Thus, the microstructure evolution from elongated to isotropic grains observed after 60 min of sintering at 250 °C may be correlated to the electrical property evolution: elongated grain shapes are associated to the presence of liquid phase contribution and increasing R_{GB} with time, while more isotropic grains are observed along with the absence of liquid phase contribution to EIS and a decrease of R_{GB} with time.

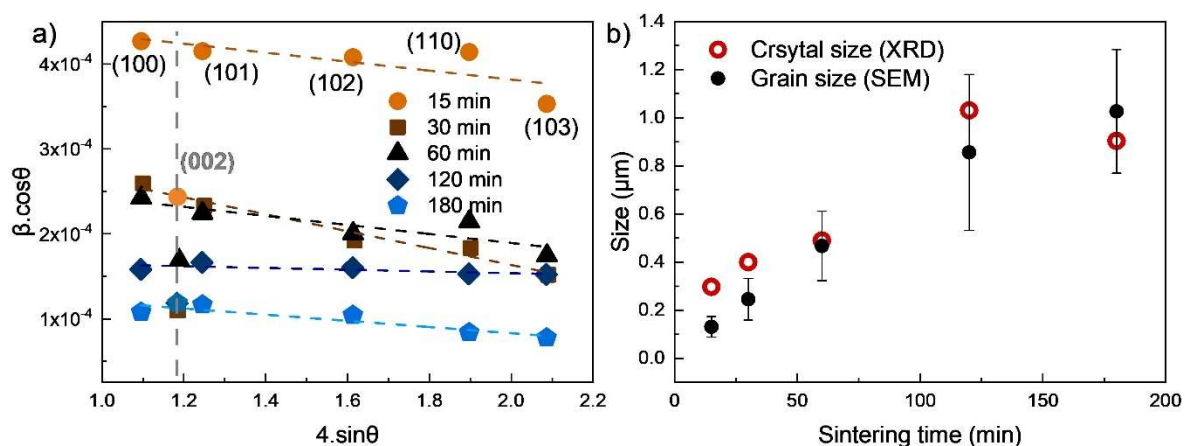


Figure 7: a) Williamson-Hall plot of samples sintered during various sintering times at 250 °C. b) Grain size/crystal size vs. sintering time determined by SEM images and XRD respectively. Error bars on grain sizes data correspond to grains size standard deviation.

XRD was performed on crushed pellets and as sintered pellets (to confirm the absence of crushing effect on XRD) for samples sintered at 250 °C during various times. Data obtained for crushed pellets (Figure S4) were fitted and plotted in Williamson-Hall plot (Figure 7a) (where β is the full width at half maximum - FWHM). Six peaks can be observed on the XRD patterns ($30 < 2\theta < 65^\circ$) corresponding to (100), (002), (101), (102), (110) and (103) planes. For all samples, Williamson-Hall data can be linearly fitted, except the (002) peak. Indeed, this one has a much lower $\beta \cdot \cos\theta$ value than the other peaks. Since $\beta \cdot \cos\theta$ is inversely proportional to crystal size [25,26], it is consistent with the observation of oriented crystal where preferred growth occurs along (001). As sintering time increases, the anisotropy decreases until (002) aligns with the other (hkl) at 180 min, which is consistent with the SEM observations. According to the Williamson-Hall plot fitting, crystal size was obtained from the Y axis intercept of the linear fitting (without considering (002) peak) for each sample and plotted on Figure 7b, and compared with grain sizes determined from SEM images. Although XRD data determination of crystal size loses accuracy as the size increases, these data

globally confirm the constant grain/crystal size evolution with sintering time, and do not show a particular event after 70 min of sintering.

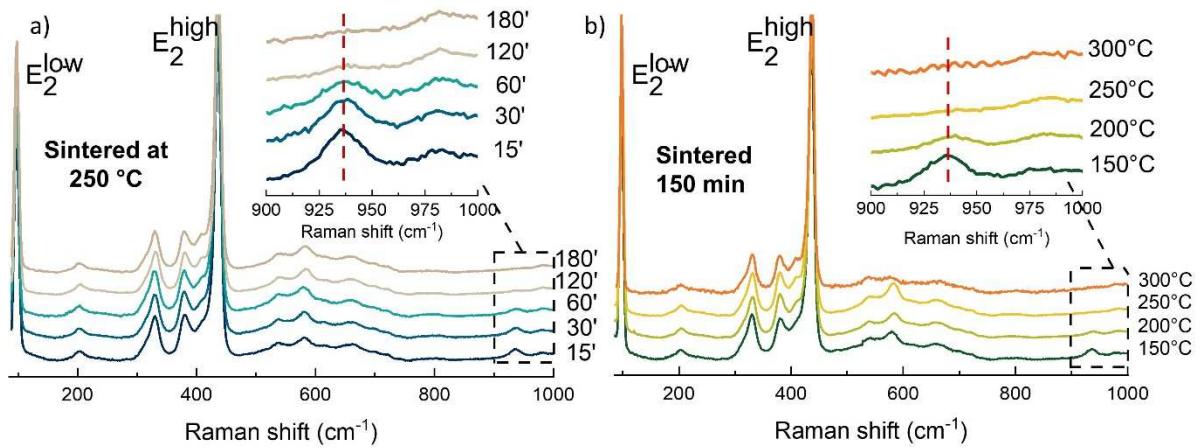


Figure 8: Raman spectra of samples sintered a) at 250 °C during various sintering times, and b) sintered during 150 min at various temperatures. Insets correspond to magnification of the 900-1000 cm^{-1} region.

Raman spectroscopy was also performed on the same powders obtained from crushed pellets that were analyzed by XRD. Additional samples were analyzed, those prepared at various temperatures from 150 to 300 °C during 150 min. The results are presented on Figure 8. All samples show the expected contributions of ZnO wurtzite phase [27,28]. Additionally, a band is visible at 935 cm^{-1} (see inset). This Raman band can be associated to acetate C-C bond stretching [29]. From Figure 8a, the C-C stretching band, resulting from the acetate presence, is present after 15 min sintering, and slowly decreases after 30 and 60 min. When the sintering is performed during 120 min, acetate contribution almost disappeared from Raman spectrum, and after 180 min, it is totally absent. The sintering temperature dependence in Figure 8b shows the same evolution, i.e. the acetate contribution is present after a 150 min sintering at 150 and 200 °C, but it is absent after 250 and 300 °C sintering. This acetate elimination at 250 °C between 60 and 120 min is consistent with EIS data showing no direct electrical contact between the two electrodes at low frequency before 60 min, confirming the presence of the liquid phase containing acetates.

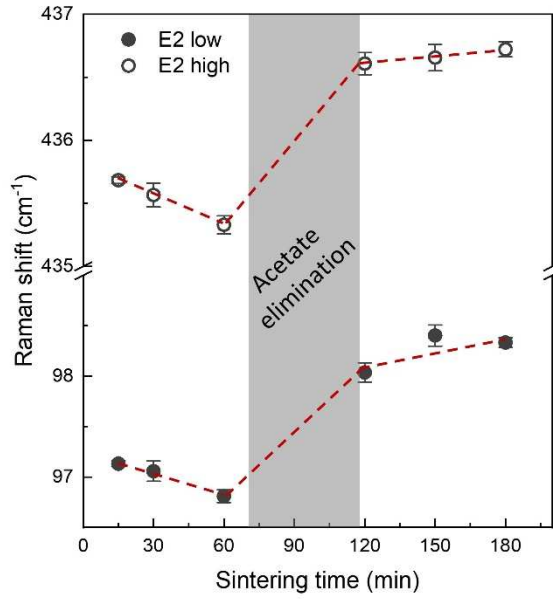


Figure 9: Raman spectra peak positions of E_2^{low} and E_2^{high} . Error bars correspond to standard deviation, red dashed line is a guide for the eyes.

Further Raman spectra analyzes were performed by fitting all peaks assuming pure Lorentzian shapes. Three spectra were recorded on all samples at various random locations to check sample's homogeneity, and the average of the three fitted band positions was plotted on Figure 9 for E_2^{high} and E_2^{low} . Both these two bands correspond to Zn and O sublattices respectively [27,28,30]. In both cases, the Raman shift decreases from 15 to 60 min, and steps up to a higher value after 120 min. Eventually, no major evolution is observed from 120 to 180 min. These observations result from Zn and O environment modification during sintering. The two observed domains are concomitant with acetate elimination previously observed. Thus, it is clear that acetate has an influence on the ZnO local environment, probably creating vacancies and locally breaking wurtzite structure [20] as suggested by Gonzalez-Julian *et al.* [20].

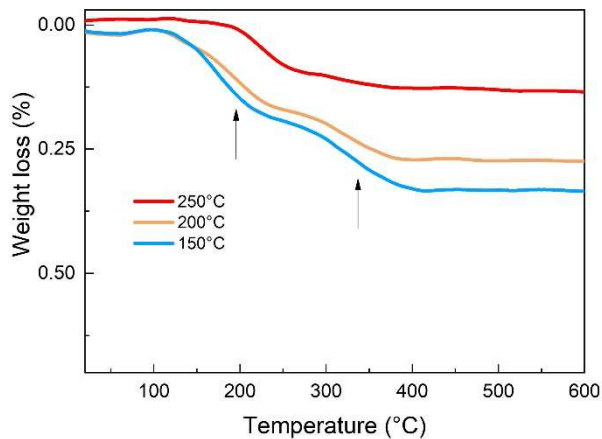


Figure 10: TGA analyzes of samples sintered during 150 min at 150, 200 and 250 °C

Thermal analyzes performed on the samples sintered at 150, 200 and 250 °C are presented on Figure 10. They are consistent with those previously presented by Funahashi *et al.* on cold sintered ZnO [16] showing two mass losses (indicated by arrows). The first one, from 150 to 250 °C was associated by mass spectrometry to water elimination, while the second one from 300 to 400 °C corresponds to acetate elimination. In the present data, a first mass loss is observed for all samples, but the second mass loss is only present for the samples sintered < 250 °C. However, these mass losses remain low: for the samples sintered at 150 and 200 °C acetate loss only represents 0.09 wt.% and 0.13 wt.%, showing the small amount of liquid required for densification.

4. Discussion

The interest of using EIS during sintering experiment is to *in situ* track the impedance change, which can be assigned to chemical or microstructural events occurring during sintering. Here the main observation is the evolution of electrical behavior when sintering is performed at 250 °C during more than 60 min, with the vanishing of the liquid phase impedance semi-circle associated to R_{GB} decrease while sintering time increases. Various hypotheses were explored concerning the origin of this event. While relative density appears not to be related, microstructural shape changes in the same period, from oriented (≤ 60 min) to isotropic grain shapes (≥ 60 min), which is observed both at grain level (SEM) and crystal level (XRD). In the meantime, Raman spectroscopy shows that acetate species are eliminated at the same time (between 60 and 120 min). It also shows that this elimination has an influence on the Zn and O sublattices (E_2^{low} and E_2^{high} position shifts), most probably by rearranging the wurtzite structure in the absence of acetate. The acetate loss at 250 °C is confirmed by TGA analyzes showing almost no weight loss between 250 and 350 °C, where both samples sintered < 250 °C show 0.09 and 0.13 wt.% losses.

To explain the R_{GB} decrease of the sample sintered at 250 °C (after 60 min), two main phenomena may be involved. First, the grain growth occurring with increasing sintering time decreases the number of grain boundaries interfaces, which would result in total GB resistance decrease. Figure S5 shows SEM images of samples sintered at 150 and 200 °C at various stages (30, 60 and 180 min), and Figure S6 summarizes grain size evolution versus sintering time for all three temperatures. The evolution is constantly increasing for 150, 200 and 250 °C, suggesting that R_{GB} decrease (observed only for 250 °C sintering) cannot be explained only by the decrease of GB number in the material. Another possibility deals with the modification of GB chemistry, associated with the observed elimination of acetates.

Figure S7 shows the GB relaxation time evolution versus sintering time for the 3 samples sintered at 150, 200 and 250 °C. While it constantly increases for the samples sintered at 150 and 200 °C, the sample sintered at 250 °C shows the similar behavior as the one observed in R_{GB} , i.e. an increase during 60 min followed by a decrease after 60 min. The evolution of this relaxation time suggests a chemical evolution of GB, even after acetate removal. Therefore, the R_{GB} decrease after 60 min at 250 °C must arise from a combination of the two phenomena: grain growth inducing a decrease of GB quantity, and chemical modification of the GB interfaces.

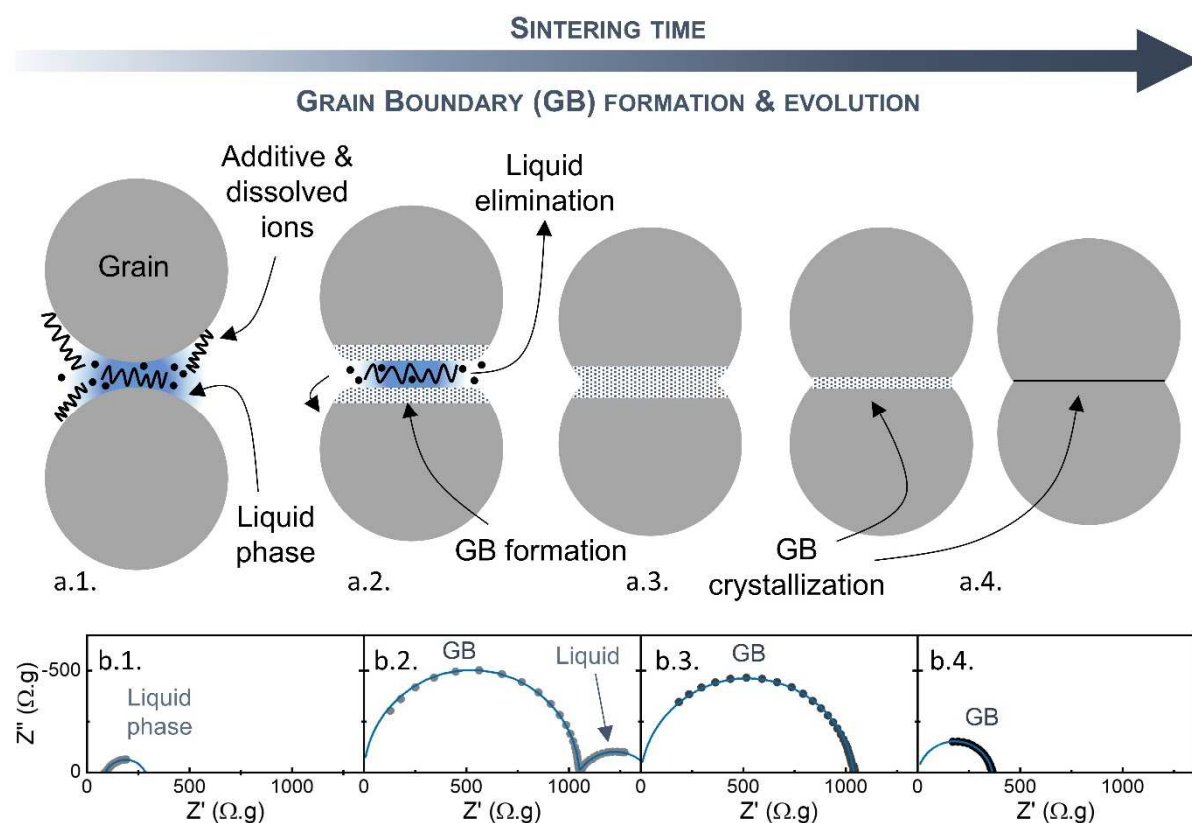


Figure 11: Schematic representation of grain boundary formation showing 4 stages (a1 to a4 on top), and the corresponding EIS Nyquist plots (b.1 to b.4). See text for details.

Thus, it is possible to determine 3 sintering stages based the observations made here (sketched on Figure 11).

Stage I: Initially, grains come into contact under pressure. They are in contact with water and dissolved acetates. While temperature increases, water is slowly eliminated and acetate start to dissolve ZnO surfaces. This stage mostly occurs during the heating stage (Figure 11 a.1). Here, only the liquid phase contributes to impedance, since grain boundaries are not yet formed (b.1).

Stage II: While temperature reaches the target sintering temperature, water is mostly eliminating (see TGA of sample sintered at 150 °C on Figure 10 and EIS data for ZnO in pure water on Figure 4b showing R_{GB} increase followed by a stabilization) and grain boundaries start forming (a.2). Two semi-circles are visible in EIS data (b.2), corresponding to these forming grain boundaries and the acetate modified interfaces. Due to the presence of acetate, grain growth preferentially occurs along the wurtzite c axis [24] and the ZnO network is modified (as observed in Raman on Figure 9). This is probably linked to defect generation such as O vacancies or interstitials [20], resulting in grain boundary resistance increase. This situation may remain stable if acetates aren't eliminated. This is the case of samples sintered < 250 °C, even when sintering time is prolonged to 360 min. This results in the observation of two semi-circles in EIS data during the whole dwell time.

Stage III: In case where the temperature allows acetate elimination, the material under sintering enters stage 3 (a.3). The first event associated to acetate elimination is its electrical resistance (R_L) disappearance, leading to a single measured semi-circle associated to grain boundaries (b.3). Concerning the microstructure, grain growth continues, but now without acetate species. Thus, grain and crystal growth become isotropic, leading to more and more isotropic grains as sintering continues. This is confirmed by XRD data on Williamson-Hall plots (Figure 7) showing (002) peak alignment with the other (hkl) peaks after acetate elimination. Eventually, Raman spectroscopy shows E_2^{low} and E_2^{high} positions shifts, resulting from a modification of local environment, and then stabilizes. By further increasing sintering time (120 to 180 min) the electrical grain boundaries resistance gradually decreases (b.4), linked to both grain boundary number decrease and their re-crystallization, eventually leading to grain boundary size reduction.

5. Conclusions

The development of *in situ* characterization techniques is detrimental for the determination of implied mechanisms. This is particularly complex for processes under important mechanical pressure since such as pressure assisted sintering techniques since the use of a die to mediate that pressure prevents direct observations. Here we developed an adapted technique to characterize by electrochemical impedance spectroscopy a material being cold sintered. A major advantage of such technique is its capacity to separate various contributions, such as bulk, grain boundaries, interfaces, etc. In the present work, it was possible to determine the

conditions for acetate elimination during sintering, while no obvious physical bulk parameter could highlight its influence on resulting ceramic (no major densification, nor particular grain growth). Previous works made on cold sintered ZnO [21,31,32] showed different electrical conductivities without explanation found for it. The use of EIS *in situ* characterization helps understanding the various sintering stages and help determine the appropriate sintering conditions to obtain a desired property (oriented microstructure, conductivity, etc.).

Although this was applied to a semiconductor material, it is also applicable for other materials families, such as capacitors such as (Ba,Sr)TiO₃, but also ceramic-polymer composites [33]. Recent work deal with the use of chelating agents to control densification and growth [9,10] during the Cold Sintering Process. The use of EIS characterization allows to follow the presence and evolution of interfaces along sintering, offering a better control on their sintering.

6. References

- [1] J. Guo, R. Floyd, S. Lowum, J.-P. Maria, T. Herisson De Beauvoir, J.H. Seo, C.A. Randall, Cold Sintering: Progress, Challenges, and Future Opportunities, Annual Review of Materials Research. 49 (2019) 275–95. <https://doi.org/10.1146/annurev-matsci-070218-010041>.
- [2] K. Nur, T.P. Mishra, J.G.P. da Silva, J. Gonzalez-Julian, M. Bram, O. Guillon, Influence of powder characteristics on cold sintering of nano-sized ZnO with density above 99 %, J Eur Ceram Soc. 41 (2021) 2648–2662. <https://doi.org/10.1016/j.jeurceramsoc.2020.11.007>.
- [3] A. Ndayishimiye, M.Y. Sengul, T. Sada, S. Dursun, S.H. Bang, Z.A. Grady, K. Tsuji, S. Funahashi, A.C.T. van Duin, C.A. Randall, Roadmap for densification in cold sintering: Chemical pathways, Open Ceramics. 2 (2020) 100019. <https://doi.org/10.1016/j.oceram.2020.100019>.
- [4] A. Kabir, M. Espineira-Cachaza, E.M. Fiordaliso, D. Ke, S. Grasso, B. Merle, V. Esposito, Effect of cold sintering process (CSP) on the electro-chemo-mechanical properties of Gd-doped ceria (GDC), J Eur Ceram Soc. 40 (2020) 5612–5618. <https://doi.org/10.1016/j.jeurceramsoc.2020.06.010>.
- [5] K. Thabet, E. Quarez, O. Joubert, A. Le Gal La Salle, Application of the cold sintering process to the electrolyte material BaCe_{0.8}Zr_{0.1}Y_{0.1}O_{3-δ}, J Eur Ceram Soc. 40 (2020) 3445–3452. <https://doi.org/10.1016/j.jeurceramsoc.2020.03.043>.
- [6] H. Guo, J. Guo, A. Baker, C.A. Randall, Cold Sintering Process for ZrO₂ -Based Ceramics: Significantly Enhanced Densification Evolution in Ytria-Doped ZrO₂, Journal of American Ceramic Society. 100 (2017) 491–495. <https://doi.org/10.1111/jace.14593>.
- [7] M. Biesuz, G. Taveri, A.I. Duff, E. Olevsky, D. Zhu, C. Hu, S. Grasso, A theoretical analysis of cold sintering, Advances in Applied Ceramics. 119 (2020) 75–89. <https://doi.org/10.1080/17436753.2019.1692173>.

- [8] J. Guo, X. Zhao, T. Herisson De Beauvoir, J.H. Seo, S.S. Berbano, A.L. Baker, C. Azina, C.A. Randall, Recent Progress in Applications of the Cold Sintering Process for Ceramic–Polymer Composites, *Advanced Functional Materials*. 28 (2018) 1801724. <https://doi.org/10.1002/adfm.201801724>.
- [9] S. Funahashi, E. Kobayashi, M. Kimura, K. Shiratsuyu, C.A. Randall, Chelate complex assisted cold sintering for spinel ceramics, *Journal of the Ceramic Society of Japan*. 127 (2019) 899–904. <https://doi.org/10.2109/jcersj2.19160>.
- [10] T. Sada, A. Ndayishimiye, Z. Fan, Y. Fujioka, C.A. Randall, Surface modification of BaTiO₃ with catechol surfactant and effects on cold sintering, *Journal of Applied Physics*. 129 (2021) 184102. <https://doi.org/10.1063/5.0049905>.
- [11] T. Herisson De Beauvoir, K. Tsuji, X. Zhao, J. Guo, C.A. Randall, Cold Sintering of ZnO-PTFE: utilizing polymer phase to promote ceramic anisotropic grain growth, *Acta Materialia*. 186 (2020) 511–516. <https://doi.org/10.1016/j.actamat.2020.01.002>.
- [12] A.J. Allen, I. Levin, R.A. Maier, S.E. Witt, F. Zhang, I. Kuzmenko, In situ characterization of ceramic cold sintering by small-angle scattering, *Journal of the American Ceramic Society*. 104 (2021) 2442–2448. <https://doi.org/10.1111/jace.17664>.
- [13] J.T.S. Irvine, D.C. Sinclair, A.R. West, *Electroceramics: Characterization by Impedance Spectroscopy*, *Advanced Materials*. 2 (1990) 132–138. <https://doi.org/10.1002/adma.19900020304>.
- [14] M. Andres-Verges, A.R. West, Impedance and Modulus Spectroscopy of ZnO Varistors, *Journal of Electroceramics*. 1 (1997) 125–132. <https://doi.org/10.1023/A:1009906315725>.
- [15] D.C. Sinclair, A.R. West, Impedance and modulus spectroscopy of semiconducting BaTiO₃ showing positive temperature coefficient of resistance, *Journal of Applied Physics*. 66 (1989) 3850–3856. <https://doi.org/10.1063/1.344049>.
- [16] S. Funahashi, J. Guo, H. Guo, K. Wang, A.L. Baker, K. Shiratsuyu, C.A. Randall, Demonstration of the Cold Sintering Process Study for the Densification and Grain Growth of ZnO Ceramics, *Journal of the American Ceramic Society*. 100 (2017) 546–553. <https://doi.org/10.1111/jace.14617>.
- [17] J. Buckeridge, C.R.A. Catlow, M.R. Farrow, A.J. Logsdail, D.O. Scanlon, T.W. Keal, P. Sherwood, S.M. Woodley, A.A. Sokol, A. Walsh, Deep vs shallow nature of oxygen vacancies and consequent n -type carrier concentrations in transparent conducting oxides, *Physical Review Materials*. 2 (2018) 56–59. <https://doi.org/10.1103/PhysRevMaterials.2.054604>.
- [18] H. Liu, G. Piret, B. Sieber, J. Laureyns, P. Roussel, W. Xu, R. Boukherroub, S. Szunerits, Electrochemical impedance spectroscopy of ZnO nanostructures, *Electrochemistry Communications*. 11 (2009) 945–949. <https://doi.org/10.1016/j.elecom.2009.02.019>.

- [19] J. Jose, M.A. Khadar, Impedance spectroscopic analysis of ac response of nanophase ZnO and ZnO-Al₂O₃ nanocomposites, *Nanostructured Materials*. 11 (1999) 1091–1099. [https://doi.org/10.1016/S0965-9773\(99\)00399-2](https://doi.org/10.1016/S0965-9773(99)00399-2).
- [20] J. Gonzalez-Julian, K. Neuhaus, M. Bernemann, J. Pereira da Silva, A. Laptev, M. Bram, O. Guillon, Unveiling the mechanisms of cold sintering of ZnO at 250 °C by varying applied stress and characterizing grain boundaries by Kelvin Probe Force Microscopy, *Acta Materialia*. 144 (2018) 116–128. <https://doi.org/10.1016/j.actamat.2017.10.055>.
- [21] Y. Jing, N. Luo, S. Wu, K. Han, X. Wang, L. Miao, Y. Wei, Remarkably improved electrical conductivity of ZnO ceramics by cold sintering and post-heat-treatment, *Ceramics International*. 44 (2018) 20570–20574.
- [22] M.J. Verkerk, B.J. Middelhuis, A.J. Burggraaf, Effect of grain boundaries on the conductivity of high-purity ZrO₂-Y₂O₃ ceramics, *Solid State Ionics*. 6 (1982) 159–170.
- [23] M.Y. Sengul, J. Guo, C.A. Randall, A.C.T. van Duin, Water-Mediated Surface Diffusion Mechanism Enables the Cold Sintering Process: A Combined Computational and Experimental Study, *Angewandte Chemie International Edition*. 58 (2019) 12420–12424. <https://doi.org/10.1002/anie.201904738>.
- [24] B. Dargatz, J. Gonzalez-Julian, O. Guillon, Anomalous coarsening of nanocrystalline zinc oxide particles in humid air, *Journal of Crystal Growth*. 419 (2015) 69–78. <https://doi.org/10.1016/j.jcrysgro.2015.02.101>.
- [25] A. Khorsand Zak, W.H. Abd. Majid, M.E. Abrishami, R. Yousefi, X-ray analysis of ZnO nanoparticles by Williamson-Hall and size-strain plot methods, *Solid State Sciences*. 13 (2011) 251–256. <https://doi.org/10.1016/j.solidstatesciences.2010.11.024>.
- [26] D. Nath, F. Singh, R. Das, X-ray diffraction analysis by Williamson-Hall, Halder-Wagner and size-strain plot methods of CdSe nanoparticles- a comparative study, *Materials Chemistry and Physics*. 239 (2020) 122021. <https://doi.org/10.1016/j.matchemphys.2019.122021>.
- [27] R. Cuscó, E. Alarcón-Lladó, J. Ibáñez, L. Artús, J. Jiménez, B. Wang, M.J. Callahan, Temperature dependence of Raman scattering in ZnO, *Physical Review B*. 75 (2007) 165202. <https://doi.org/10.1103/PhysRevB.75.165202>.
- [28] M. Šćepanović, M. Grujić-Brojčín, K. Vojisavljević, S. Bernikc, T. Srećković, Raman study of structural disorder in ZnO nanopowders, *Journal of Raman Spectroscopy*. 41 (2010) 914–921. <https://doi.org/10.1002/jrs.2546>.
- [29] M.M. Yang, D.A. Crerar, D.E. Irish, A Raman spectroscopic study of lead and zinc acetate complexes in hydrothermal solutions, *Geochimica et Cosmochimica Acta*. 53 (1989) 319–326. [https://doi.org/10.1016/0016-7037\(89\)90384-0](https://doi.org/10.1016/0016-7037(89)90384-0).

- [30] K.A. Alim, V.A. Fonoberov, M. Shamsa, A.A. Balandin, Micro-Raman investigation of optical phonons in ZnO nanocrystals, *Journal of Applied Physics*. 97 (2005) 124313. <https://doi.org/10.1063/1.1944222>.
- [31] X. Zhao, J. Guo, K. Wang, T. Herisson De Beauvoir, B. Li, C.A. Randall, Introducing a ZnO-PTFE (Polymer) Nanocomposite Varistor via the Cold Sintering Process, *Advanced Engineering Materials*. 20 (2018) 1700902. <https://doi.org/10.1002/adem.201700902>.
- [32] T. Hérisson de Beauvoir, K. Tsuji, X. Zhao, J. Guo, C. Randall, Cold sintering of ZnO-PTFE: Utilizing polymer phase to promote ceramic anisotropic grain growth, *Acta Materialia*. 186 (2020). <https://doi.org/10.1016/j.actamat.2020.01.002>.
- [33] T. Sada, K. Tsuji, A. Ndayishimiye, Z. Fan, Y. Fujioka, C.A. Randall, Enhanced high permittivity BaTiO₃ – polymer nanocomposites from the cold sintering process, *Journal of Applied Physics*. 128 (2020) 084103. <https://doi.org/10.1063/5.0021040>.